Mie scattering analysis of spherical Bragg "onion" resonators

Wei Liang, Yong Xu, Yanyi Huang, and Amnon Yariv

Department of Applied Physics, California Institute of Technology, Pasadena, CA 91125
liangwei@its.caltech.edu

J. G. Fleming, and Shawn-Yu Lin

Sandia National Laboratories, Albuquerque NM 87185-1080

Abstract: Combining the Mie scattering theory and a transfer matrix method, we investigate in detail the scattering of light by spherical Bragg "onion" resonators. We classify the resonator modes into two classes, the core modes that are confined by Bragg reflection, and the cladding modes that are confined by total internal reflection. We demonstrate that these two types of modes lead to significantly different scattering behaviors.

References and links

1. A. Ashkin and J. M. Dziedzic, "Observation of Resonances in the Radiation Pressure on Dielectric Spheres," Phys. Rev. Lett. **38**, 1351-1355 (1977).
2. Petr Chylek, J. T. Kiehl, and M. K. W. Ko, "Optical levitation and partial-wave resonances," Phys. Rev. A. **18**, 2229-2233, (1978).
3. V.B.Braginsky, M. L. Gorodetsky, and V.S. Ilchenko, "Quality-factor and nonlinear properties of optical whispering-gallery modes," Phys. Lett. A. **137**, 393-396 (1989).
4. Craig F. Bohren, Donald R. Huffman, *Absorption and Scattering of Light by Small Particles*, (John Wiley & Sons, Inc, 1998).
5. Kerry J. Vahala, "Optical microcavities," Nature **424**, 839-846, (2003).
6. M. Cai, G. Hunziker, and K. Vahala, "Fiber-optic add/drop device based on a silica microsphere-whispering gallery mode system," IEEE Photon. Technol. Lett. **11**, 686–687, (1999).
7. M. Cai, P.O. Hedekvist, A. Bhardwaj, K. Vahala, "5-Gbit/s BER performance on an all fiber-optic add/drop device based on a taper-resonator-taper structure," IEEE Photon. Technol. Lett. **12**, 1177-1179, (2000).
8. D.W. Vernooy, A. Furusawa, N. P. Georgiades, V. S. Ilchenko, and H. J. Kimble, "Cavity QED with high-Q whispering gallery modes," Phys. Rev. A. **57**, R2293 (1998).
9. J. R. Buck and H. J. Kimble, "Optimal sizes of dielectric microspheres for cavity QED with strong coupling," Phys. Rev. A. **67**, 033806 (2003).
10. Z. S. Wu, L. X. Guo, K. F. Ren, G. Gouesbet, and G. Grehan, "Improved algorithm for electromagnetic scattering of plane waves and shaped beams by multilayered spheres," Appl. Opt. **36**, 5188-5198 (1997).
11. Kevin G. Sullivan and Dennis G. Hall, "Radiation in spherically symmetric structure. I. the coupled-amplitude equations for vector spherical waves," Phys. Rev. A. **50**, 2701-2707, (1994).
12. David D. Smith, Kirk A. Fuller, "Photonic bandgaps in Mie scattering by concentrically stratified spheres," J. Opt. Soc. Am. B. **19**, 2449-2455, (2002).
13. Yong Xu, Wei Liang, Amnon Yariv, J. G. Fleming, and Shawn-Yu Lin, "High quality factor Bragg onion resonators with omnidirectional reflector cladding," Opt. Lett. **28**, 2144-2146, (2003).
14. Yong Xu, Wei Liang, Amnon Yariv, J. G. Fleming, and Shawn-Yu Lin, "Modal analysis of spherically symmetric Bragg resonators," to appear in Opt. Lett.
15. G. Mie, ''Beitrâge zur optik truber Medien, speziell kolloidaler Metallosungen,''Ann. Phys. **25**, 377–452 (1908).
16. John David Jackson, *Classical Electrodynamics*, (John Wiley & Sons, Inc, Third Edition, 1999), Chap. 10.
17. G. Gouesbet, B. Maheu, and G. Grehan, "Light scattering from a sphere arbitrarily located in a Gaussian beam, using a Bromwich formulation," J. Opt. Soc. Am. A **5**, 1427-1442, (1988).

18.   J. A Lock and G. Gouesbet, "Rigorous justification of the localized approximation to the beam-shape coefficients in generalized Lorenz-Mie theory. I. On-axis beams," J. Opt. Soc. Am. A **11**, 2503-2515, (1994).

19.   M. L. Gorodetsky and V. S. IIchenko, "Optical microsphere resonators: optimal coupling to high-Q whispering-gallery modes," J. Opt. Soc. Am. B **16**, 147-154, (1999).

20.   U. Fano, "Effects of configuration interaction on intensities and phase shifts," Phys. Rev. **124**, 1866-1878, (1961).

1. Introduction

Dielectric microspheres, which can support whispering-gallery modes with quality factors as high as 10^9, have been extensively investigated since the 1970's [1-5]. Recently, they have been proposed for many potentially important applications in wavelength division multiplexing (WDM) (as add-drop filters) [6,7], and in cavity quantum electrodynamics (QED) [8,9]. A common tool in characterizing properties of the dielectric microspheres is through the measurement of light scattering by the microspheres. Typically, the scattering spectrum exhibits many sharp, well-defined peaks, which can be traced to the presence of the high Q whispering gallery modes. From the position and the width of such spectral peaks, we can extract the resonant frequencies and quality factors of the corresponding whispering-gallery modes.

Besides total internal reflection, it is also possible to construct a multi-layer dielectric sphere and use Bragg reflection to confine light in the spherical cavity. In the literature, there have been a few theoretical discussions about spherically symmetric Bragg resonators [10-12]. In a recent publication, we proposed to approximate the completely spherically symmetric Bragg resonator with an onion-shaped spherical Bragg resonator [13,14]. The onion resonator has been realized at Sandia National Laboratories through a fabrication procedure combining etching and chemical vapor deposition (CVD). A scanning electron microscope (SEM) image of the onion resonator is shown in Fig. 1.
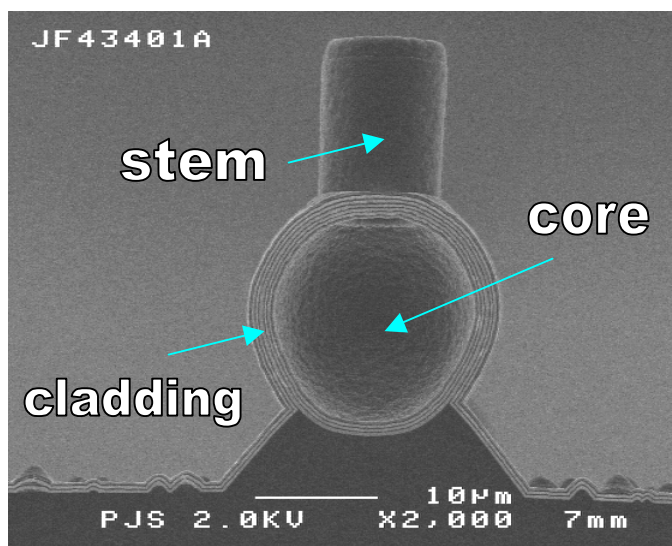

Fig. 1. A SEM image of the onion resonator.

As in the case of dielectric microspheres, through investigating the scattering of the Bragg onion resonators, we can infer useful information about the properties of the onion resonator modes. In Ref. [14], we have shown that onion resonator modes can in general be classified into two types, the Fabry-Perot type core modes, and the whispering-gallery type cladding modes. The core modes are confined by the cladding Bragg reflection and are mostly

concentrated within the onion core region. The confinement mechanism for the cladding modes, on the other hand, is total internal reflection. Consequently, the cladding modes are mostly distributed within the cladding layers of the onion resonators. Later in this paper, we will demonstrate that the scattering resonances of these two different types of modes have distinctively different scattering characteristics.

The paper is organized as follows: In section II, we present a transfer matrix theory for the calculation of the scattering spectrum of Bragg onion resonators (assuming a plane wave as the incident wave). With a slight modification, the transfer matrix formalism can also be applied to the more realistic cases where the incident wave has a Gaussian beam profile (as in most optical scattering measurements). In section III, we apply the transfer matrix theory and calculate the scattering spectra of the Bragg onion resonators. We discuss various significant features of the Bragg onion resonator scattering spectra. We conclude this paper in section IV.

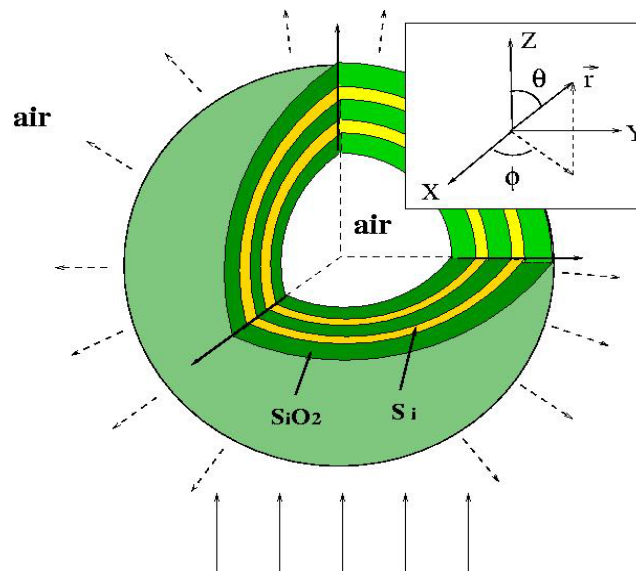## 2. Theory of light scattering by a multilayer sphere

Fig. 2. Light scattering by a spherical Bragg "onion" resonator.

In order to obtain analytical formulas for the scattering parameters of the onion resonator, we ignore the presence of onion stem (as shown in Fig. 1) and assume that the onion structure possesses complete spherical symmetry. Under this assumption, we can label the onion resonator mode according to the angular quantum number l [13,14]. Furthermore, we can classify the onion resonator modes as either TE polarized or TM polarized, where the electrical field of the TE mode and the magnetic field of the TM mode only have transverse components (along the $\hat{e}_\theta$ and $\hat{e}_\varphi$ direction).

The Mie scattering theory, which was developed over almost a hundred years ago [15], has been used extensively for the scattering analysis of dielectric microspheres. After incorporating some results from a transfer matrix theory, we can apply directly the original Mie scattering theory to the case of Bragg onion resonators. We begin our analysis by assuming that the incident wave is a plane wave at frequency $\omega/2\pi$ with unit amplitude and polarized along the x direction. The incident wave can be expanded in terms of various multipole moments:[16]

$$\vec{E}_{inc} = \hat{e}_x e^{ikz} = \sum_{l=1}^{\infty} i^l \frac{\sqrt{4\pi(2l+1)}}{2}\left[j_l(kr)(\vec{X}_{l,+1}+\vec{X}_{l,-1}) + \frac{1}{k}\vec{\nabla}\times j_l(kr)(\vec{X}_{l,+1}-\vec{X}_{l,-1}) \right] \quad (1)$$

where $\vec{X}_{l,m} = 1/i\cdot\vec{r}\times\vec{\nabla}Y_{lm}(\theta,\phi)/\sqrt{l(l+1)}$ is the normalized vectorial spherical harmonic function (the angular parameters θ and φ are defined in Fig. 2), $k=\omega/c$ is the wave vector and $j_l(kr)$ is the lth order spherical Bessel function. Without a loss of generality, the scattered field can also be expanded in the form of:

$$\vec{E}_{sc}^{x} = \sum_{l=1}^{\infty} i^l \frac{\sqrt{4\pi(2l+1)}}{2}\left[\frac{\alpha_l}{2} h_l^1(kr)(\vec{X}_{l,+1}+\vec{X}_{l,-1}) + \frac{\beta_l}{2}\frac{\vec{\nabla}}{k}\times h_l^1(kr)(\vec{X}_{l,+1}-\vec{X}_{l,-1}) \right] \quad (2)$$

Where $h_l^1(kr)$ is the lth order spherical Hankel function of the first kind and the parameters α_l, β_l are, respectively, the scattering coefficients for the TE and the TM components.

In far-field region, where $kr \gg l$, the scattered field as given in Eq. (2) can be simplified to:

$$\vec{E}_{sc}^{x} \approx \frac{ie^{ikr}}{kr}(\cos\phi\cdot S_2(\theta)\hat{e}_\theta - \sin\phi\cdot S_1(\theta)\hat{e}_\phi) \quad (3)$$

where

$$S_2(\theta) = \sum_{l=1}^{\infty} \frac{(2l+1)}{l(l+1)}\left(\frac{\alpha_l}{2}\frac{P_l^1}{\sin\theta} + \frac{\beta_l}{2}\frac{dP_l^1}{d\theta} \right)$$

$$S_1(\theta) = \sum_{l=1}^{\infty} \frac{(2l+1)}{l(l+1)}\left(\frac{\alpha_l}{2}\frac{dP_l^1}{d\theta} + \frac{\beta_l}{2}\frac{P_l^1}{\sin\theta} \right)$$

$$(4)$$

In Eq. (4), P_l^1 is the associated Legendre function.

From Eq. (3), we find that the differential scattering cross section, which is defined as the optical power scattered into a unit solid angle and normalized by the intensity of the input wave, is given by:

$$\frac{d\sigma_{sc}}{d\Omega} = \frac{dP_{sc}}{I_{inc}d\Omega} = \frac{\frac{1}{2}\cdot c\varepsilon_0\left|\vec{E}_{sc}^{x}\right|^2\cdot r^2}{\frac{1}{2}\cdot c\varepsilon_0\left|\vec{E}_{inc}\right|^2}$$

$$= \frac{1}{k^2}\left(|S_2|^2\cos^2\phi + |S_1|^2\sin^2\phi \right) \quad (5)$$

The total scattering cross section can be obtained from Eq. (5) by integrating the differential cross-section over the entire 4π solid angle [16]:

$$\sigma_{total} = -\frac{\pi}{k^2}\sum_{l=1}^{\infty}(2l+1)\mathrm{Re}[\alpha_l + \beta_l] \quad (6)$$

From Eq. (6), we can easily find the total scattering cross-section once we know the coefficients α_l and β_l for all orders of partial waves. In the following discussion, we outline a transfer matrix method developed in reference [13] and apply it to the calculation of the scattering coefficient α_l and β_l. To begin our analysis, it suffices to consider a single partial

wave with quantum number (l, m), since the incident wave and the scattered wave, as given in Eq. (1) and (2), are formed from linearly independent combinations of components with different l and m ($m = \pm 1$). For the lth order TE or TM multipole components within the nth dielectric layer, we can express the corresponding electromagnetic field as:

$$
\begin{bmatrix} \vec{H} \\ \vec{E} \end{bmatrix} = \begin{bmatrix} j_l(k_n r)\vec{X}_{l,m} & h_l^1(k_n r)\vec{X}_{l,m} \\ Z_n \dfrac{i}{k_n}\vec{\nabla}\times j_l(k_n r)\vec{X}_{l,m} & Z_n \dfrac{i}{k_n}\vec{\nabla}\times h_l^1(k_n r)\vec{X}_{l,m} \end{bmatrix} \cdot \begin{bmatrix} A_n \\ B_n \end{bmatrix} \quad \text{(TM)} \qquad (7a)
$$

$$
\begin{bmatrix} \vec{E} \\ \vec{H} \end{bmatrix} = \begin{bmatrix} j_l(k_n r)\vec{X}_{l,m} & h_l^1(k_n r)\vec{X}_{l,m} \\ \dfrac{-i}{Z_n k_n}\vec{\nabla}\times j_l(k_n r)\vec{X}_{l,m} & \dfrac{-i}{Z_n k_n}\vec{\nabla}\times h_l^1(k_n r)\vec{X}_{l,m} \end{bmatrix} \cdot \begin{bmatrix} C_n \\ D_n \end{bmatrix} \quad \text{(TE)} \qquad (7b)
$$

where $Z_n = \sqrt{\mu_0 / \varepsilon_0 \varepsilon_n}$ is the material impedance and $k_n = \sqrt{\varepsilon_n}\,\omega/c$. The four linear coefficients A_n, B_n, C_n, and D_n are constant within the nth layer. Employing the continuity condition of $E_\theta, E_\phi, H_\theta, H_\phi$ at the interface between two adjacent layers and the orthogonality of the spherical harmonics, we can relate the linear coefficients A_n, B_n, C_n, and D_n in the nth layer to those in the $(n+1)$th layer through the following matrix relations:

$$
\begin{bmatrix} j_l(k_n r_n) & h_l^1(k_n r_n) \\ \dfrac{Z_n}{k_n}\dfrac{\partial}{\partial r}[rj_l(k_n r)]\Big|_{r_n} & \dfrac{Z_n}{k_n}\dfrac{\partial}{\partial r}[rh_l^1(k_n r)]\Big|_{r_n} \end{bmatrix}\begin{pmatrix} A_n \\ B_n \end{pmatrix} =
$$
$$
\begin{bmatrix} j_l(k_{n+1} r_n) & h_l^1(k_{n+1} r_n) \\ \dfrac{Z_{n+1}}{k_{n+1}}\dfrac{\partial}{\partial r}[rj_l(k_{n+1} r)]\Big|_{r_n} & \dfrac{Z_{n+1}}{k_{n+1}}\dfrac{\partial}{\partial r}[rh_l^1(k_{n+1} r)]\Big|_{r_n} \end{bmatrix}\begin{pmatrix} A_{n+1} \\ B_{n+1} \end{pmatrix} \qquad \text{(TM)} \quad (8a)
$$

$$
\begin{bmatrix} j_l(k_n r_n) & h_l^1(k_n r_n) \\ \dfrac{1}{Z_n k_n}\dfrac{\partial}{\partial r}[rj_l(k_n r)]\Big|_{r_n} & \dfrac{\partial}{Z_n k_n \partial r}[rh_l^1(k_n r)]\Big|_{r_n} \end{bmatrix}\begin{pmatrix} C_n \\ D_n \end{pmatrix} =
$$
$$
\begin{bmatrix} j_l(k_{n+1} r_n) & h_l^1(k_{n+1} r_n) \\ \dfrac{\partial}{Z_{n+1} k_{n+1}\partial r}[rj_l(k_{n+1} r)]\Big|_{r_n} & \dfrac{\partial}{Z_{n+1} k_{n+1}\partial r}[rh_l^1(k_{n+1} r)]\Big|_{r_n} \end{bmatrix}\begin{pmatrix} C_{n+1} \\ D_{n+1} \end{pmatrix} \qquad \text{(TE)} \quad (8b)
$$

Applying Eq (8) iteratively, we find that the linear coefficients in the core area (A_{co}, B_{co}, C_{co}, D_{co}) can be expressed in terms of those in the outside free space (A_{out}, B_{out}, C_{out}, D_{out}) as

$$
\begin{bmatrix} A_{co} \\ B_{co} \end{bmatrix} = M_l^{TM} \cdot \begin{bmatrix} A_{out} \\ B_{out} \end{bmatrix} \qquad \text{(TM)}
$$
$$
\begin{bmatrix} C_{co} \\ D_{co} \end{bmatrix} = M_l^{TE} \cdot \begin{bmatrix} C_{out} \\ D_{out} \end{bmatrix} \qquad \text{(TE)}
$$
$$
(9)
$$

In Eq. (9), the two matrices M_l^{TM} and M_l^{TE} are obtained from multiplying and dividing a series of two by two matrices given in Eq. (8a) and (8b). In labeling M_l^{TM} and M_l^{TE}, we drop the quantum number m since the matrices are identical for components with the same l but different m.

Combining Eqs. (1), (2), and (9), we can derive a simple expression for scattering coefficients α_l and β_l. First, we notice that the total electromagnetic field outside the onion resonator is the sum of the incident wave and the scattered wave ($\vec{E}_{total} = \vec{E}_{inc} + \vec{E}_{sc}$), which gives:

$$\vec{E}_{tot} = \sum_{l=1}^{\infty} i^l \frac{\sqrt{4\pi(2l+1)}}{2}\left[(j_l + \frac{\alpha_l}{2}h_l^1)(\vec{X}_{l,+1} + \vec{X}_{l,-1}) + \frac{\vec{\nabla}}{k}\times(j_l + \frac{\beta_l}{2}h_l^1)(\vec{X}_{l,+1} - \vec{X}_{l,-1}) \right] \quad (10)$$

Meanwhile according to Eq. (7), outside of the onion resonator, the electromagnetic field for the component with quantum number *(l, m)* is given by:

$$\vec{E}_{tot}^{l,m} \propto \vec{\nabla}\times\left[(A_{out}j_l(kr) + B_{out}h_l^1(kr))\vec{X}_{l,m} \right] \quad \text{(TM)} \qquad (11a)$$

$$\vec{E}_{tot}^{l,m} \propto (C_{out}j_l(kr) + D_{out}h_l^1(kr))\vec{X}_{l,m} \qquad \text{(TE)} \qquad (11b)$$

Comparing Eqs. (11a) and (11b) with Eq. (10), we find:

$$A_{out}/B_{out} = 2/\beta_l , \ C_{out}/D_{out} = 2/\alpha_l \qquad (12)$$

We emphasize that this relation is valid for all multipole orders. Furthermore, we notice that a physical solution must have finite value at the origin, which leads to

$$B_{co} = (M_l^{TM})_{2,1}A_{out} + (M_l^{TM})_{2,2}B_{out} = 0 \qquad (13a)$$

$$D_{co} = (M_l^{TE})_{2,1}C_{out} + (M_l^{TE})_{2,2}D_{out} = 0 \qquad (13b)$$

Combining Eq. (12) and Eq. (13), we immediately find

$$\beta_l/2 = -(M_l^{TM})_{2,1}/(M_l^{TM})_{2,2}$$
$$\alpha_l/2 = -(M_l^{TE})_{2,1}/(M_l^{TE})_{2,2} \qquad (14)$$

Once α_l and β_l are obtained, we can find the scattering cross-section of the *l*th order partial wave and the total scattering cross-section from Eq. (6).

The procedure for the calculation of scattering cross-section as outlined above applies to cases where incident wave is a plane wave. In experiments, though, the incident wave is likely to have a Gaussian beam profile. The case of a Gaussian incident wave can be analyzed using the generalized Mie theory [17,18], where the effect of a Gaussian beam can be included by multiplying the scattering coefficients $\alpha_{l,m}$ and $\beta_{l,m}$ by a beam shape factor $g_{l,TE}^m$ for TE modes or $g_{l,TM}^m$ for TM modes. In this paper, we limit ourselves to the simplest case where the center of the onion resonator coincides with the center of the waist plane of a fundamental Gaussian beam. In this case, the factors $g_{l,TE}^m$ and $g_{l,TM}^m$ are reduced to the same factor g_l [18]:

$$g_l = \exp\left\{ -\left[\frac{(l+1/2)\lambda}{2\pi W_0} \right]^2 \right\} \qquad (15)$$

where W_0 is the radius of the minimal spot of the fundamental Gaussian beam, λ is the wavelength.

To describe the scattering spectrum of the onion resonator, it is often convenient to use a dimensionless parameter, the total scattering efficiency, which is defined as the ratio between the total scattering cross section σ_{total} and the area of the onion resonator cross-section:

$$Q_{tot}^{scatt} = \frac{\sigma_{total}}{\pi R^2} = -\frac{1}{k^2 R^2} \sum_{l=1}^{\infty} (2l+1) \operatorname{Re}[\alpha_l + \beta_l] \qquad (16)$$

In this definition, R is the radius of entire onion resonator. Similarly, we can define the differential scattering efficiency as $dQ_{tot}^{scatt}/d\Omega = d\sigma_{sc}/\pi R^2 d\Omega$, with $d\sigma_{sc}/d\Omega$ given by Eq. (5). In the following section, all numerical results are given in terms of scattering efficiency instead of scattering cross-section.

3. Numerical result and discussion

In this section, we discuss the scattering spectra of a representative Bragg onion resonator, which is composed of an air core of radius $r_{co} = 7\mu m$, followed by a SiO$_2$ layer and N_{clad} pairs of Si/SiO$_2$ Bragg cladding layers. The thickness of all SiO$_2$ layers is $L_{sio_2} = 0.258\mu m$, and the refractive index is $n_{sio_2} = 1.5$. Correspondingly, for Si layers, we have $L_{si} = 0.111\mu m$ and $n_{si} = 3.5$. We limit ourselves within the wavelength range of $1.51\sim1.59\,\mu m$. The bandgap center of the onion cladding is located at $1.55\,\mu m$.
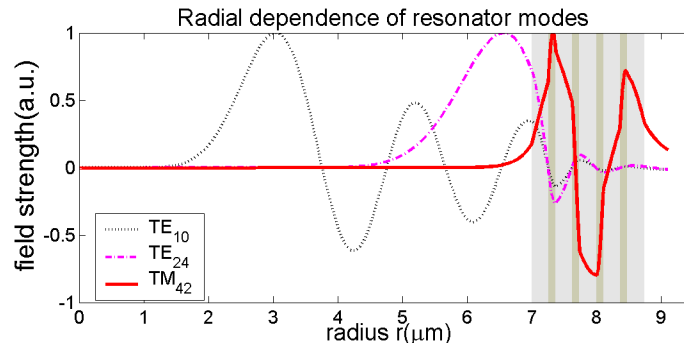

Fig. 3. Radial dependence of the electrical field of TE mode and the magnetic field of TM mode.
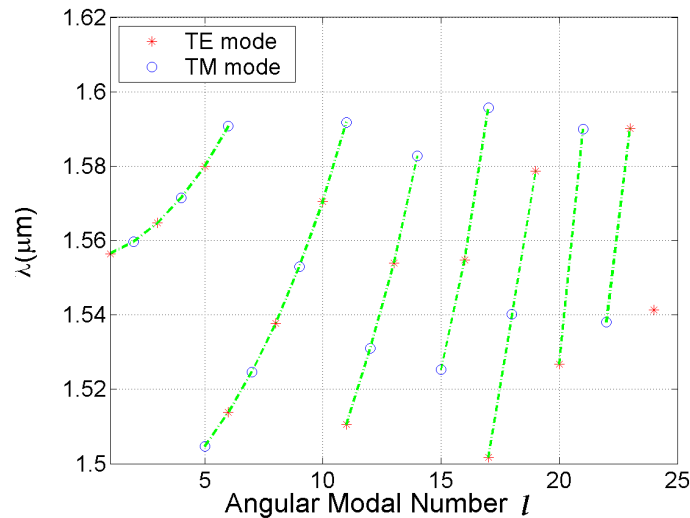

Fig. 4. Spectrum of the onion resonator modes (calculated with $N_{clad} = 4$).

Before calculating the scattering spectrum of the onion resonators, we first summarize some important properties of the onion resonator modes. As mentioned earlier, the onion resonator modes can be classified into core modes and cladding modes. The core modes possess relatively small angular quantum number l and are of the Fabry-Perot type. Their field distribution is mostly confined within the onion air core. In contrast, the cladding modes have large angular quantum number l and are similar to the whispering-gallery modes in disk resonators. The electromagnetic fields of the cladding modes are concentrated within the cladding layers. In Fig. 3, we show the radial dependence of the transverse components (transverse electrical field of TE mode or transverse magnetic field of TM mode) of a cladding mode (TM_{42}) and two core modes (TE_{10} and TE_{24}). We use parameters of the onion resonator given in the previous paragraph and choose $N_{clad} = 4$. The features in Fig. 3 clearly demonstrate the different localization of modal energy of the two types of modes. In Fig. 4, we plot the spectrum of the core modes within the wavelength range of $1.51 \sim 1.59\,\mu m$. Similar to what has been shown in Ref. [14], we can classify the core modes into distinctive groups, as indicated by the dashed lines in Fig. 4.
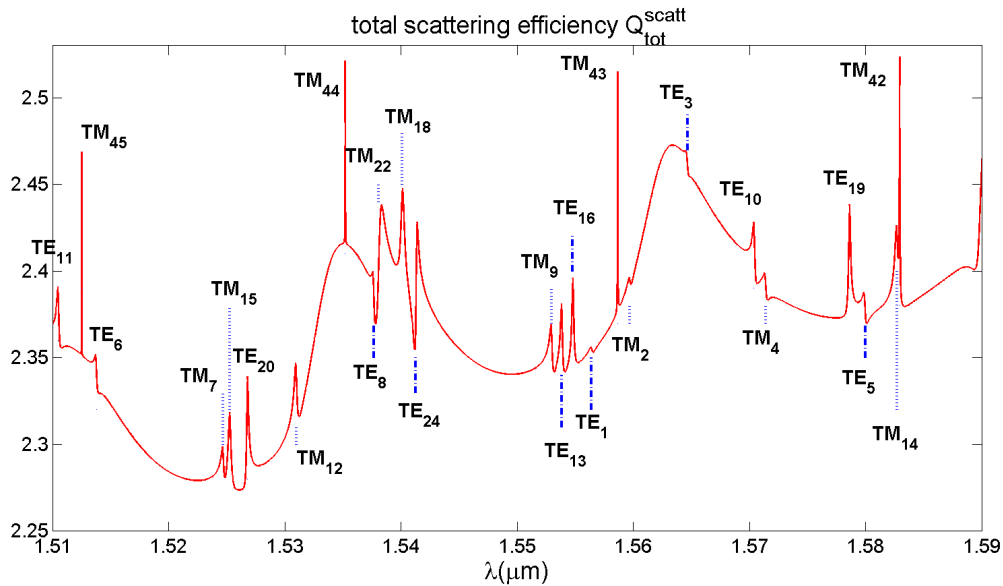

Fig. 5. Spectrum of total scattering efficiency. The number of Bragg pairs is $N_{clad} = 4$.

The scattering spectrum of the previously discussed onion resonator is shown in Fig. 5. In the calculation, we assume an incident plane wave and take $N_{clad} = 4$. In the figure, the location of TE and TM mode frequencies are indicated with dashed lines. From the scattering spectrum, it is clear that there are significant differences between resonances due to the cladding modes and those due to the core modes. All together, Fig. 5 has four scattering peaks that correspond respectively to the TM_{42}, TM_{43}, TM_{44}, and TM_{45} cladding modes. Their scattering resonances are more pronounced in amplitude as compared with those of the core modes. On the other hand, the core mode resonances exhibit more complicated spectral features. To further illustrate the difference between cladding mode resonances and core mode resonances, we study TE_{10}, TE_{24}, TM_{42} and TM_{43} modes as examples.

We use the scattering formalism developed in section II to calculate $-Re(\beta_l)$, the real part of the lth order scattering coefficient, for the TM_{42} and TM_{43} mode. The results are given in

Fig. 6(a) and Fig. 6(b) as solid dots. Since we are mainly interested in the resonant part of the scattering coefficient, in calculating $-\text{Re}(\beta_l)$, we respectively choose $l=42$ for the TM_{42} mode and $l=43$ for the TM_{43} mode. As in the case of whispering-gallery modes of a silica microsphere [19], the resonant scattering coefficient shown in Fig. 6(a) and Fig. 6(b) can be well approximated by a Lorentzian line-shape [19]:

$$-\text{Re}(\alpha \text{ or } \beta) = \frac{2}{1 + (Q \cdot 2\Delta\lambda/\lambda_0)^2} \tag{17}$$

where Q and λ_0 are respectively the quality factor and the wavelength of the cavity mode, and $\Delta\lambda$ is defined as $\Delta\lambda = \lambda - \lambda_0$. In Fig. 6(a) and Fig. 6(b), we plot the approximate Lorentzian line-shape as given by Eq. (17) (shown as solid lines). We emphasize that the Lorentzian approximation is not obtained from numerically fitting the "exact" resonant scattering coefficients. Instead, all free parameters (Q and λ_0) are directly calculated from the transfer matrix method in Ref [13]. It is remarkable to notice the extremely good agreement between the two results, even though they are generated from two different approaches without any fitting.
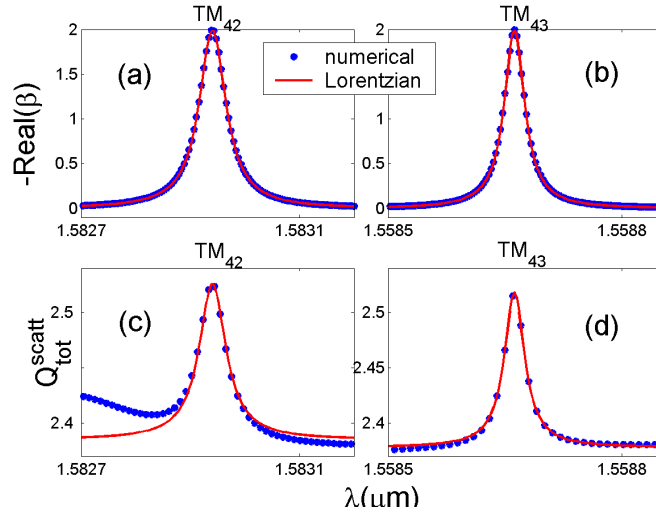

Fig. 6. Comparison of scattering resonances numerically obtained using the Mie scattering method developed in section 2, and those given by a Lorentzian approximation. The number of Bragg pair is $N_{clad} = 4$.

The total scattering efficiency of the onion resonator has contributions from both a resonant part and a non-resonant part. As a first order approximation, we can substitute Eq. (17) into Eq. (16), add a constant "background" term Q_{bg}^{scatt}, and write the total scattering efficiency near resonance as:

$$Q_{tot}^{scatt} = Q_{bg}^{scatt} + \frac{2l+1}{k^2 R^2} \frac{2}{1 + (Q \cdot 2\Delta\lambda/\lambda_0)^2} \tag{18}$$

where l is the angular quantum number of the resonant onion mode. In Eq. (18), only Q_{bg}^{scatt} is a fitting parameter, whereas Q and λ_0, as before, are all directly inferred from transfer matrix calculations. In Fig. 6(c) and Fig. 6(d), we plot the total scattering efficiency (calculated from the formalism developed in section II and represented as dots), and the approximate form

given by Eq. (18) (represented as solid lines). From Fig. 6(c) and Fig. 6(d), it is clear that the sharp peaks in the total scattering spectrum can be entirely attributed to the presence of the cladding modes, and we can accurately extract modal frequencies and quality factors from the scattering spectrum.

Significantly different from those of the cladding modes, the spectral characteristics of the core modes are asymmetric and share some similarities with those of Fano resonances [20]. From the scattering resonances shown in Fig. 5, we choose to study two representative cases that correspond to the TE_{10} and TE_{24} mode. In Fig. 7(a) and Fig. 7(c), we give, respectively, the resonant scattering coefficients $-Re[\alpha_l]$ and the total scattering efficiencies for these two modes. In the figure, the corresponding core mode wavelengths are indicated using dashed vertical lines. We notice that for the core modes, the wavelengths with maximal or minimal scattering efficiencies do not coincide with the exact modal eigenwavelengths. And unlike cladding mode cases, the core mode scattering spectra do not have the usual symmetrical Lorentzian line-shape. Instead, the scattering spectra reach the minimal (or the maximal) value first and then flip quickly to the opposite limit. We also notice that there is no definite rule regarding whether the scattering efficiency first reaches a dip or a peak. In Fig. 7(b) and Fig. 7(d), we plot the resonant scattering coefficients and the total scattering efficiencies for the same onion resonator but with $N_{clad}=5$. It is interesting to notice that the order of the appearance of the peak or the dip changes as N_{clad} increases from 4 to 5.
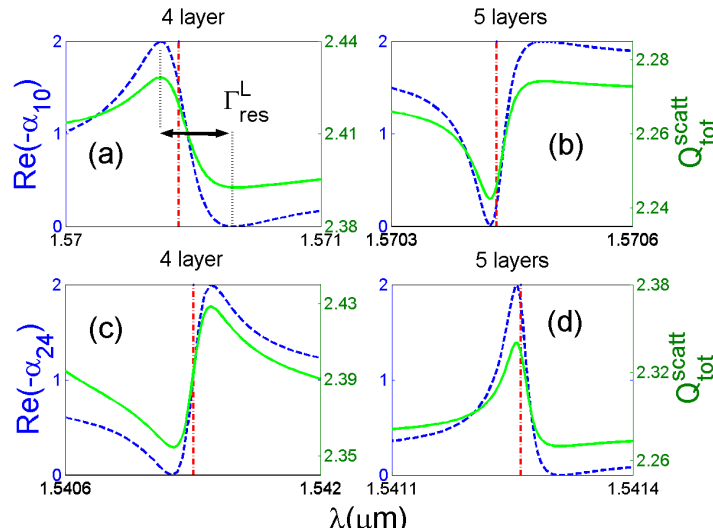

Fig. 7. Scattering resonances of the TE_{10} and TE_{24} modes (with $N_{clad} = 4$ and 5). The dashed lines represent the resonant scattering coefficient $-Re(\alpha_l)$ (whose values are shown on the left y-axis), and the solid lines represent the total scattering efficiency Q_{tot}^{scatt} (whose values are shown on the right y-axis). The dashed vertical lines give the position of modal wavelength.

In Fig. 6, we have demonstrated that for the cladding modes, we can extract modal resonant wavelengths and quality factors from their corresponding scattering resonances. For the core modes, even though their scattering spectra is no longer Lorentzian, we can still expect a definite relationship between the scattering spectrum and the corresponding modal quality factor Q. Quantitatively, we can characterize the sharpness of the core mode resonance using the modal resonance width Γ_{res}^l, which is defined as the wavelength difference between the peak and the dip in the resonant scattering coefficient spectrum (see Fig. 7(a)). Similarly,

we can define the modal resonance width Γ_{res}^{tot} for the total scattering efficiencies. In Fig. 8, we compare λ/Γ_{res}^{l}, $\lambda/\Gamma_{res}^{tot}$, and quality factors of TE_{10} and TE_{24} modes as a function of N_{clad}. For the resonance width Γ_{res}^{tot} calculated from the total scattering efficiencies, only results with $N_{clad} \geq 4$ are shown, since for smaller N_{clad}, the core modes have low quality factors and the resonance structures due to different modes merge together. From Fig. 8, it is clear that the parameter $\lambda/\Gamma_{res}^{tot}$ provides a good estimation for the core mode quality factors. As a result, we can obtain information on the core mode wavelength and its quality factor from the scattering spectrum of the onion resonator.
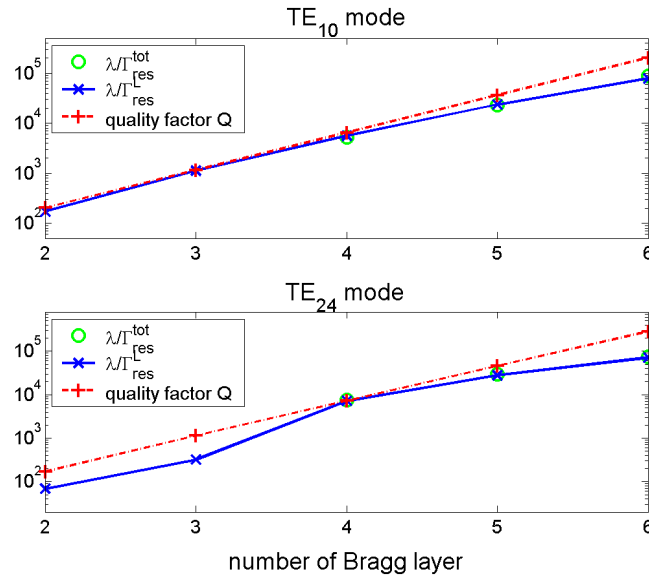

Fig. 8. Comparison of the scattering resonance width Γ_{res} and the modal quality factor as a function of the Bragg pair number. Γ_{res}^{L} and Γ_{res}^{tot} represent, respectively, the resonance width of the scattering coefficient $-\text{Re}(\alpha)$ and the total scattering efficiency Q_{tot}^{scatt} (see Fig. 7(a)).

For the onion resonator shown in Fig. 1, the fabrication process can introduce a finite amount of absorption in the silicon layers. We can account for material absorption by introducing an imaginary part ε_i to the Si dielectric constant. Experimental evidences suggest that Si layer absorption is of the order of dB/cm, which corresponds to a value of $\varepsilon_i \sim 10^{-4}$. Since the cladding modes are mostly confined in the cladding region and the core modes mostly within the air core, we expect that the presence of Si absorption will have bigger impact on the cladding modes. In Fig. 9, we compare the resonance structure of TE_{24} and TM_{42} modes for three different values of ε_i: 0, 1e-4 and 1e-3. As expected, the influence of absorption loss is indeed more pronounced for the cladding mode than the core mode.
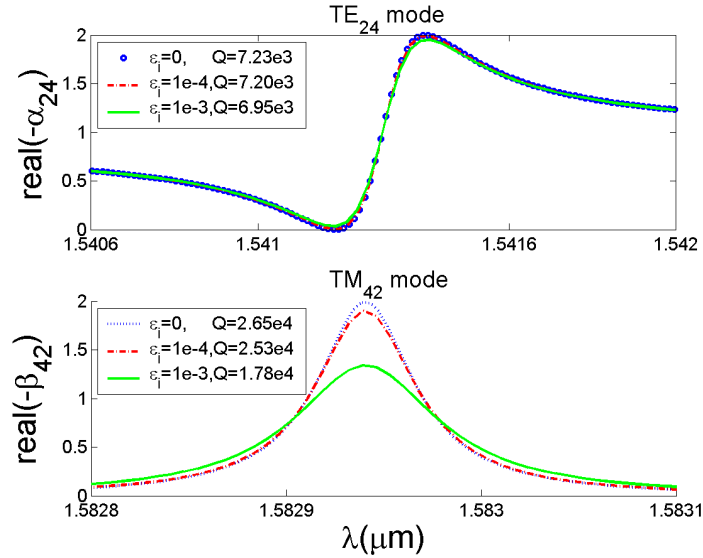
Fig. 9. Effect of absorption on scattering resonances. The number of Bragg pairs is $N_{clad} = 4$.

Finally we consider two issues related to the experimental measurement of scattering spectrum. As discussed previously, the input wave in actual measurements is likely to be a Gaussian beam, which can be accounted through multiplying the scattering coefficients α_l and β_l by the beam shape factor g_l given in Eq. (15). In Fig. 10(a), we compare the scattering spectrum of a plane wave incident on an onion resonator with $N_{clad} = 4$ with that of a Gaussian incident wave. We assume that the center of the minimal beam spot of the Gaussian beam coincides with the onion core center, and use a minimal beam width of 5 μm in the calculation. In Fig. 10(a), it is interesting to notice that the Gaussian incident wave eliminates the scattering resonances due to the cladding modes (i.e., TM_{42}, TM_{43}, TM_{44}, and TM_{45}). On the other hand, using a Gaussian incident beam does not have a significant impact on the core mode scattering resonances. Mathematically, this difference between the core mode and the cladding mode can be attributed to the fact that the beam shape factor g_l, as given in Eq. (15), clearly favors modes with smaller angular quantum number l (i.e., core modes). From more physical point of view, for an input Gaussian beam with a smaller beam width, we expect a lower coupling between the input Gaussian wave and the onion cladding modes, since the cladding modes concentrate in the region relatively further from the center of the onion resonator.

In experiments, it is often difficult to collect light scattered by the onion resonator into the entire 4π solid angle. Instead, we consider a more realistic scenario where the back-reflected light within the range of $0.9\pi \leq \theta \leq \pi$ is collected. The corresponding scattering spectrum can be obtained from integrating the differential scattering cross-section for $0 \leq \varphi \leq 2\pi$ and $0.9\pi \leq \theta \leq \pi$. In Fig. 10(b), we show two back-scattering spectra that correspond to the two cases investigated in Fig. 10(a) (one with plane incident wave and the other one with a Gaussian incident wave). As in Fig. 10(a), we find that using the Gaussian incident wave suppresses the resonances due to the cladding modes. Comparing Fig. 10(a) with Fig. 10(b), we notice that for a few core modes, the shapes of the total scattering spectrum and the back-scattering spectrum are different. However, we can still determine the wavelength of the core modes from the sharp variations of the back-scattering spectrum.
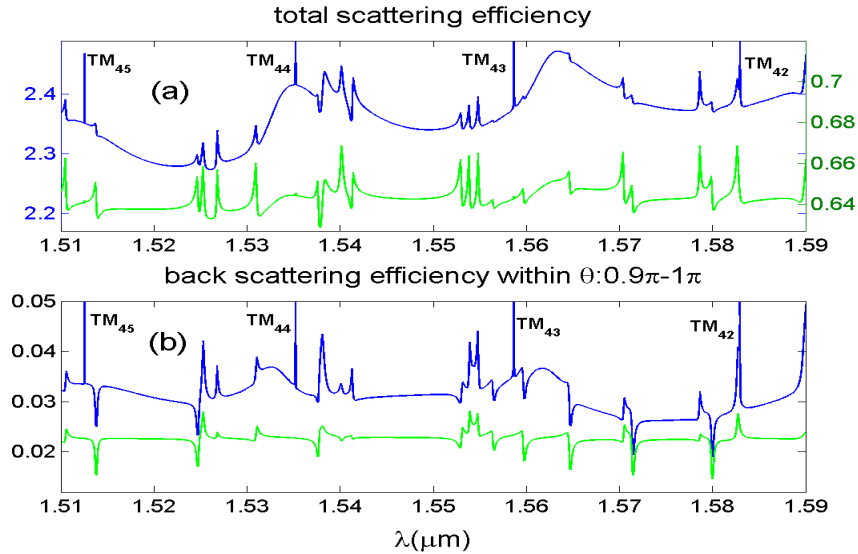
Fig. 10.Comparison between plane and Gaussian incident wave. In both (a) and (b), the upper line is under the assumption the incident wave is a plane wave; the lower one is under the assumption the incident wave is a Gaussian beam with the waist width of 5 μm with the sphere located at the center of the beam. In (a), the values of the upper and lower lines are shown on the left and right *y*-axis respectively. The number of Bragg pair is $N_{clad} = 4$.

4. Conclusion

We combine the Mie scattering theory and a transfer matrix method to analyze light scattering by a spherical Bragg onion resonator. We present and analyze numerical results for several representative cases. We find the scattering resonances due to the core modes differ significantly from those of the cladding modes. We also demonstrate that the detailed shape of the scattering spectrum depends on factors such as the incident beam profile and the scheme for the collection of scattered light. Particularly in the case the sphere is located at the center of the beam, the cladding modes can be eliminated by shrinking the spot size of the Gaussian beam while the influence on core modes is not significant. We conclude that the wavelength and the quality factor of the onion resonator modes can be obtained from the position and sharpness of the resonances in the scattering spectrum.

Acknowledgments